The Astrophysical Journal, 951:37 (11pp), 2023 July 1 https://doi.org/10.3847/1538-4357/acd541

Drop in the Hard Pulsed Fraction and a Candidate Cyclotron Line in IGR J16320–4751 Seen by NuSTAR

A. Bodaghee[1], J.-L. Chiu[2], J. A. Tomsick[3], V. Bhalerao[4], E. Bottacini[5,6,7], M. Clavel[8], C. Cox[1], F. Fürst[9], M. J. Middleton[10], F. Rahoui[11], J. Rodriguez[12], P. Romano[13], and J. Wilms[14]
[1] Department of Chemistry, Physics and Astronomy, Georgia College and State University, 231 W. Hancock St., Milledgeville, GA 31061, USA
arash.bodaghee@gcsu.edu
[2] National Space Organization, National Applied Research Labs, Hsinchu City 300, Taiwan
[3] Space Sciences Laboratory, University of California, 7 Gauss Way, Berkeley, CA 94720, USA
[4] Indian Institute of Technology Bombay, Powai, Mumbai 400076, India
[5] W.W. Hansen Experimental Physics Laboratory & Kavli Institute for Particle Astrophysics and Cosmology, Stanford University, 452 Lomita Mall, Palo Alto, CA 94305, USA
[6] Dipartimento di Fisica e Astronomia "G. Galilei," Università di Padova, Via Belzoni 7, I-35131 Padova, Italy
[7] Eureka Scientific, 2452 Delmer St., Ste. 100, Oakland, CA 94602, USA
[8] Université Grenoble Alpes, CNRS, IPAG, F-38000 Grenoble, France
[9] Quasar Science Resources SL for ESA, European Space Astronomy Centre (ESAC), Science Operations Department, E-28692 Villanueva de la Cañada, Madrid, Spain
[10] Department of Physics and Astronomy, University of Southampton, Highfield, Southampton SO17 1BJ, UK
[11] European Southern Observatory, Karl Schwarzchild-Strasse 2, D-85748 Garching bei Munchen, Germany
[12] Université Paris-Saclay, Université Paris Cité, CEA, CNRS, AIM, F-91191, Gif-sur-Yvette, France
[13] INAF, Osservatorio Astronomico di Brera, Via E. Bianchi 46, I-23807 Merate, Italy
[14] Dr. Karl-Remeis-Sternwarte and ECAP, Sternwartstrasse 7, D-96049 Bamberg, Germany
Received 2022 September 13; revised 2023 April 24; accepted 2023 May 11; published 2023 July 3

Abstract

We report on a timing and spectral analysis of a 50 ks NuSTAR observation of IGR J16320−4751 (= AX J1631.9 −4752), a high-mass X-ray binary hosting a slowly rotating neutron star. In this observation from 2015, the spin period was 1308.8 ± 0.4 s giving a period derivative $\dot{P} \sim 2 \times 10^{-8}$ s s^{-1} when compared with the period measured in 2004. In addition, the pulsed fraction decreased as a function of energy, as opposed to the constant trend that was seen previously. This suggests a change in the accretion geometry of the system during the intervening 11 yr. The phase-averaged spectra were fit with the typical model for accreting pulsars: a power law with an exponential cutoff. This left positive residuals at 6.4 keV attributable to the known iron Kα line, as well as negative residuals around 14 keV from a candidate cyclotron line detected at a significance of 5σ. We found no significant differences in the spectral parameters across the spin period, other than the expected changes in flux and component normalizations. A flare lasting around 5 ks was captured during the first half of the observation, where the X-ray emission hardened and the local column density decreased. Finally, the binary orbital period was refined to 8.9912 ± 0.0078 days thanks to Swift/BAT monitoring data from 2005–2022.

Unified Astronomy Thesaurus concepts: X-ray binary stars (1811); High mass x-ray binary stars (733); Neutron stars (1108); Pulsars (1306); Compact objects (288); Massive stars (732)

1. Introduction

Hard X-ray monitoring of the Galactic plane by INTEGRAL has uncovered dozens of new high-mass X-ray binaries (HMXBs; Walter et al. 2015; Sidoli & Paizis 2018; Kretschmar et al. 2019). These are systems in which a neutron star (NS) or a black hole accretes from a massive companion star ($M \gtrsim 5\,M_{\odot}$). Given that INTEGRAL's position uncertainty is a few arcminutes, the only way to tell that these objects are HMXBs is by follow-up observations with X-ray telescopes such as Chandra, NuSTAR, Suzaku, Swift, and XMM-Newton.

During follow-up observations, many HMXBs have presented characteristics that understandably hindered their detection in lower-energy X-ray surveys. They could be extremely obscured below 5 keV with X-ray-absorbing column densities ($N_{\rm H}$) several times 10^{23} cm^{-2}, or an order of magnitude more than the cumulative Galactic absorption along the line of sight (e.g., Matt & Guainazzi 2003; Walter et al. 2003; Patel et al. 2004). Some stay at a low level of emission for months or years ($\sim 10^{32}$ erg s^{-1}) and awaken with huge flares where the luminosity would increase by up to 6 orders of magnitude (i.e., supergiant fast X-ray transients or SFXTs; in't Zand 2005; Negueruela et al. 2006; Romano et al. 2014, 2015; Bozzo et al. 2015; Sidoli et al. 2016). Finally, they could have spin periods lasting around 1 ks (e.g., Bodaghee et al. 2006; Rodriguez et al. 2006; Zurita Heras et al. 2006).

One of the obscured HMXBs detected early in the INTEGRAL mission was IGR J16320−4751 (Rodriguez et al. 2003; Tomsick et al. 2003). This turned out to be the high-energy counterpart of an unclassified X-ray source named AX J1631.9−4752 that had been discovered two years earlier by ASCA (Sugizaki et al. 2001). A coherent pulsation of 1309 ± 40 s, consistent with the spin period of an accreting NS, was measured with XMM-Newton (Lutovinov et al. 2005), and was later refined to 1303.8 ± 0.9 s (Rodriguez et al. 2006). While the source varies on short timescales, its average, hard X-ray flux since its discovery by ASCA has stayed within a narrow range (Krimm et al. 2013; Krivonos et al. 2022). Near-IR spectroscopy suggests a supergiant

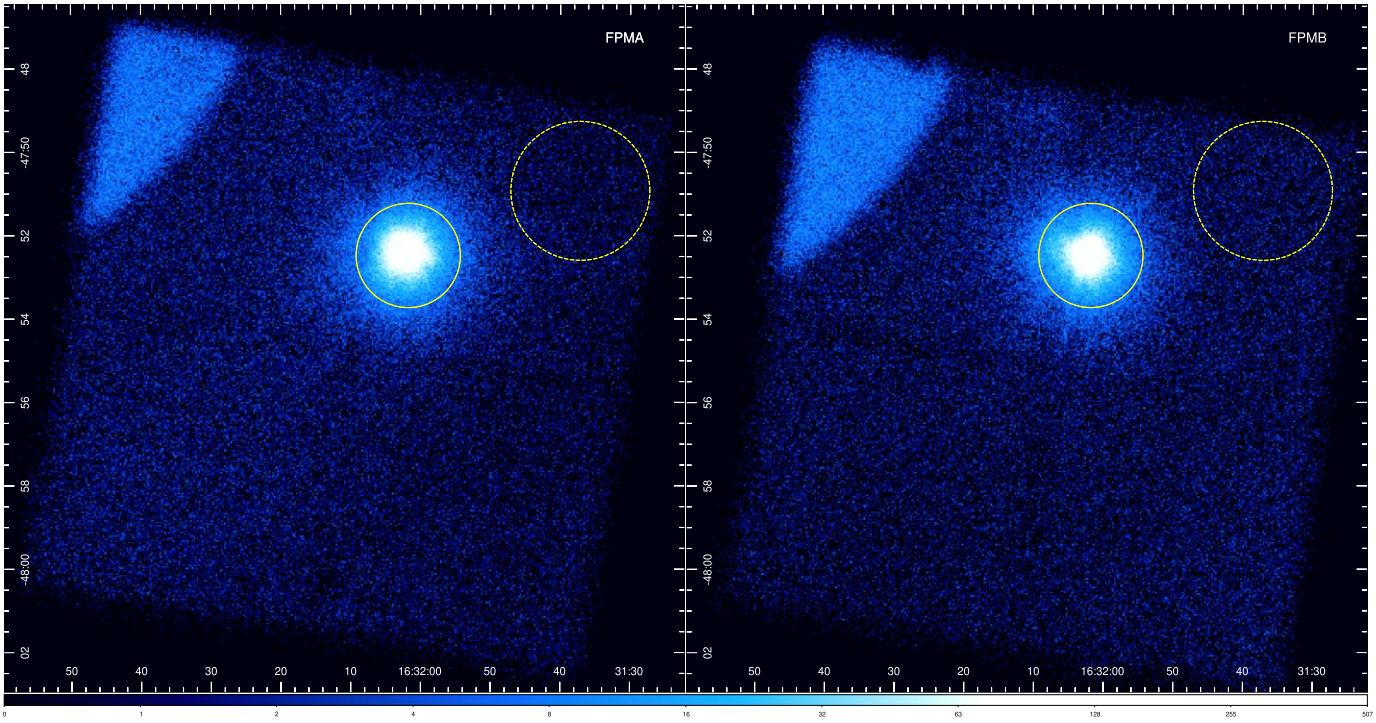

Figure 1. Images of IGR J16320−4751 gathered with NuSTAR FPMA (left) and FPMB (right) at 3–79 keV. The images are presented in J2000.0 equatorial coordinates, they are scaled logarithmically, and the extraction regions for the source (75″ radius) and background (100″ radius) are indicated.

donor star whose spectral type is BN0.5 Ia (Coleiro et al. 2013), thereby confirming its status as an HMXB at a distance of ∼3.5 kpc (Rahoui et al. 2008). Six arcminutes away from IGR J16320−4751 is an unrelated pulsar wind nebula (Acero et al. 2015) detected in the gamma rays by Fermi/LAT (4FGL J1633.0−4746e; Abdollahi et al. 2020) and HESS (HESS J1632−478; Aharonian et al. 2006).

With a short orbital period of 8.99 ± 0.01 days (Corbet et al. 2005; Levine et al. 2011; García et al. 2018), the large absorption ($N_{\rm H} \gtrsim 10^{23}$ cm^{-2}) is likely due to the NS being shrouded by the wind of its companion star. In the case of supergiant donors, the stellar wind is the main contributor to the photoelectric absorption and the Fe Kα emission (Giménez-García et al. 2015; Pradhan et al. 2018). In the specific case of IGR J16320−4751, García et al. (2018) demonstrated that these parameters as measured by XMM-Newton are modulated with the orbital period of the binary as determined by Swift/BAT, i.e., they are related to the configuration of the X-ray source and surrounding wind as viewed by the observer.

In 2015, NuSTAR pointed at IGR J16320−4751 for 29 hr and the results are presented for the first time in this paper. Procedures for analysis of the NuSTAR data are described in Section 2. Results from timing and spectral analyses are presented in Section 3, and they are discussed in Section 4.

2. Observations and Data Analysis

NuSTAR observed IGR J16320−4751 for a total of 103.6 ks from 18:46:07 (UT) on 2015 June 6 to 23:36:07 (UT) on 2015 June 7. This observation (ObsID: 30101026002) collected 49.8 ks of on-source time (good time intervals) on each of its two focal plane modules A and B (FPMA and FPMB), which have a $13' \times 13'$ field of view (FoV).

The NuSTAR data were reduced using `nupipeline` and `nuproducts` from the NuSTAR Data Analysis Software (`NuSTARDAS` v2.1.1) as distributed with `HEASoft` (v6.29; Nasa High Energy Astrophysics Science Archive Research Center (Heasarc) 2014). Response files were linked to the latest calibration database available at the time (`CALDB` 20220105). We extracted source counts for FPMA and FPMB from a circular region with a radius of 75″ centered at the source position listed in the 4XMM Serendipitous Source Catalog (Webb et al. 2020): R.A. (J2000.0) = $16^{\rm h}32^{\rm m}01\overset{\rm s}{.}76$, and decl. = $-47°52'29\overset{''}{.}0$. Background counts were extracted from a circular region (100″ radius) situated away from the source region while remaining on the same detector chip.

Figure 1 presents the field of IGR J16320−4751 from FPMA and FPMB along with the source and background extraction regions. Stray light from GX 340 + 0, situated 3° outside the FoV, affected a small portion of one detector chip from each module. The boundary of the stray light contamination region was far enough away from the location of IGR J16320−4751 that it did not impact our analysis.

A concurrent Swift/XRT observation (ObsID: 00081642001) was performed on 2015 June 6 between 20:07:38 and 22:06:56 (UT) for an effective exposure time of 1703 s. The Swift/XRT data were processed according to the standard procedure of `xrtpipeline` (v0.13.6). Source counts were extracted from inside a circular region whose radius was 20 pixels (1 pixel ∼ $2\overset{''}{.}36$). Background events were taken from an annular source-free region centered on the source (inner/outer radii of 70/110 pixels). Ancillary response files were generated with `xrtmkarf` (v0.6.3) to account for the different extraction regions, vignetting, and point-spread function corrections, while the spectral redistribution matrix was the most recent version available (20130101v014).

Light-curve data for IGR J16320−4751 were downloaded from the Swift/BAT Hard X-Ray Transient Monitor[15]

[15] https://swift.gsfc.nasa.gov/results/transients/

Table 1
Log of Observations of IGR J16320−4751

Telescope	Observation ID	Pointing R.A. (J2000)	Pointing Decl. (J2000)	Start Date (UT)	End Date (UT)	Effective Exposure (ks)
NuSTAR	30001008002	248.0277	−47.904	2015-06-06 18:46:07	2015-06-07 23:36:07	49.845
Swift/XRT	00081642001	247.9418	−47.8672	2015-06-06 20:07:38	2015-06-06 22:06:56	1.703

(Krimm et al. 2013), where the source is listed under its alias AX J1631.9−4752. These data consist of a count rate and error at 15–50 keV collected during each orbital pointing of the Swift satellite between 2005 February 14 and 2022 July 20. Data of poor quality were excluded by selecting only those rows where "`DATA_FLAG==0`." The remaining 78,882 pointings have exposure times that range from 64 s to 2.64 ks (an average of 665 s) giving a total effective exposure time of 52.5 Ms spread over 550 Ms of calendar time (6366 days).

Relying on the 4XMM position above, we performed barycentric corrections on the NuSTAR data in `nuproducts`, while the Swift XRT and BAT data were barycentered using `barycorr` with the orbital ephemeris parameter set to `geocenter`. Timing and spectral data were analyzed in `Xronos` (v6.0) and `XSpec` (v12.12.0; Arnaud 1996), respectively, with the latter assuming the elemental abundances from Wilms et al. (2000) and the photoionization cross sections from Verner et al. (1996). The NuSTAR data were restricted to 3–79 keV, the Swift/XRT data were limited to 0.3–10 keV, and known bad channels from both telescopes were ignored. The NuSTAR spectral counts were grouped such that each bin had a minimum significance of 5σ (for phase-resolved analysis) and 10σ (for phase-averaged analysis) permitting the use of χ^2 statistics, while the Swift/XRT spectral data were grouped at 20 counts per bin. Unless specified otherwise, error bars in the figures indicate 1σ confidence boundaries, while error values cited in the text and tables are given at 90% confidence. A log of NuSTAR and Swift/XRT observations is provided in Table 1.

3. Results

3.1. Timing Analysis

3.1.1. Light Curve

Figure 2 shows the NuSTAR background-subtracted light curve (3–79 keV) and hardness ratio, where the net source counts from both modules have been summed. The hardness ratio is defined as $(H-S)/(H+S)$, where S (3–10 keV) and H (10–79 keV) are the net count rates. In FPMA, there were a total of $110{,}296 \pm 333$ net counts in 49.89 ks of effective exposure time, and in FPMB, there were $98{,}064 \pm 314$ net counts in 49.84 ks. Summing the net counts from both modules returned a total of $208{,}360 \pm 458$ counts or a count rate of 4.18 ± 0.01 counts s^{-1}.

A flare lasting ∼5 ks was noticed around 22 ks into the observation. This time interval of 22–27 ks after the observation began was called the "flare" epoch. During the flare, there were $14{,}321 \pm 120$ net counts in FPMA, and $12{,}756 \pm 113$ net counts in FPMB, with an effective exposure time of 2.26 ks per module. When the modules were summed, the total net count was $27{,}078 \pm 165$ with an average count rate of 11.98 ± 0.07 counts s^{-1}.

The rest of the observation, i.e., excluding the flare, was referred to as the "nonflare" epoch. This epoch contained

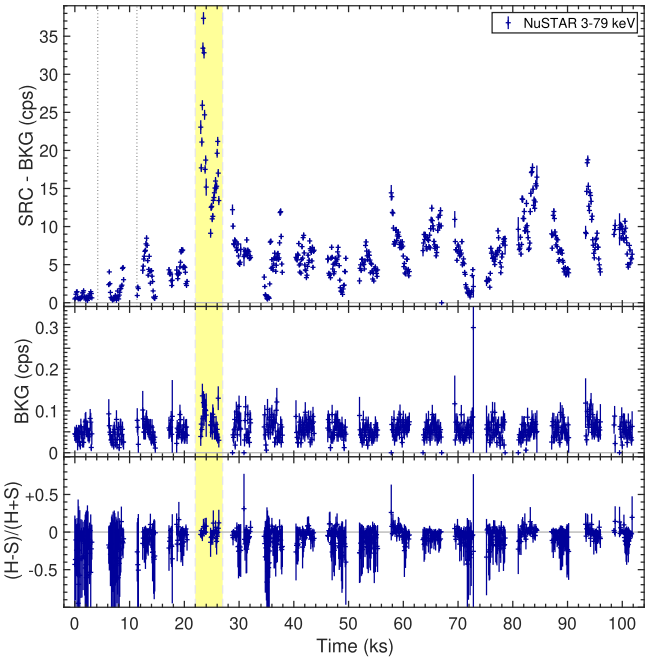

Figure 2. Light curve and hardness ratio from NuSTAR (3–79 keV) for IGR J16320−4751 with 100 s in each bin ($T_0 =$ MJD 57,179.795322). The total (FPMA+FPMB) net source count rate is presented in the top panel, where the background count rate, as shown in the middle panel, has been scaled by area and subtracted. The hardness ratio is featured in the bottom panel, where S and H represent the count rates at 3–10 keV and 10–79 keV, respectively. The flare corresponds to an epoch 22–27 ks into the observation (highlighted in light yellow and bounded by dashed lines). The dotted lines indicate the start and stop times of the contemporaneous Swift/XRT pointing.

$95{,}975 \pm 311$ net counts in FPMA (47.64 ks), and $85{,}308 \pm 293$ net counts in FPMB (47.59 ks). A sum of both modules gave $181{,}283 \pm 427$ total net counts or 3.81 ± 0.01 counts s^{-1}.

In Swift/XRT, there were 112 ± 12 net counts in 1703 s for a count rate of $(6.6 \pm 0.7) \times 10^{-2}$ counts s^{-1}.

3.1.2. Spin Period

A periodicity search was performed with `efsearch` on the source (+ background) light curve (0.1 s resolution) of the full observation in five energy bands: 3–6 keV, 6–12 keV, 12–25 keV, 25–79 keV, and 3–79 keV. A coherent pulsation near the known period of 1300 s was detected in all energy bands except 25–79 keV. The pulsation was detected most significantly at lower energies (Figure 3). Figure 4 presents the pulse profile with 20 bins per period for energies up to 25 keV. In the 3–6 keV band, the best-fitting period was 1308.8 ± 0.4 s, where the centroid was determined with the Press & Rybicki (1989) fast algorithm for Lomb–Scargle periodograms (Lomb 1976; Scargle 1982) and the error from Horne & Baliunas (1986) and Leahy (1987).

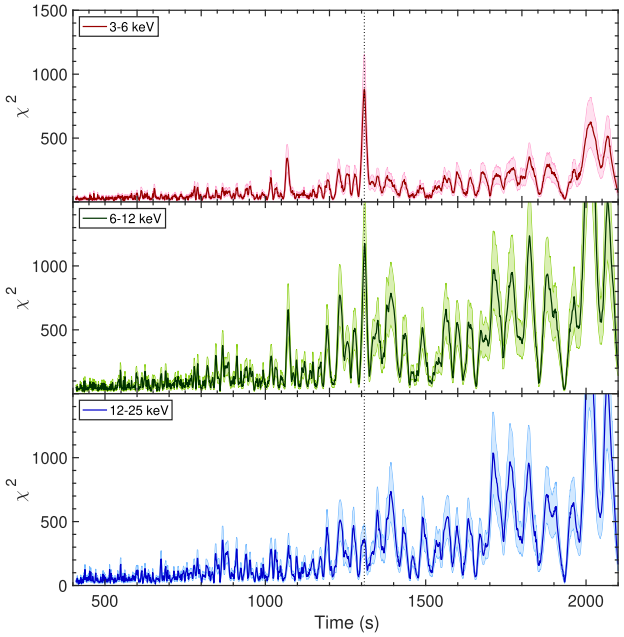

Figure 3. Spin period search (χ^2 distribution) on the NuSTAR light curve of IGR J16320−4751 with 20 bins per period and a resolution of 1.2 s in three energy bands: 3–6 keV (top panel, red curve), 6–12 keV (middle panel, green curve), and 12–25 keV (bottom panel, blue curve). The best-fitting spin period ($P = 1308.8$ s) is denoted by a dotted line.

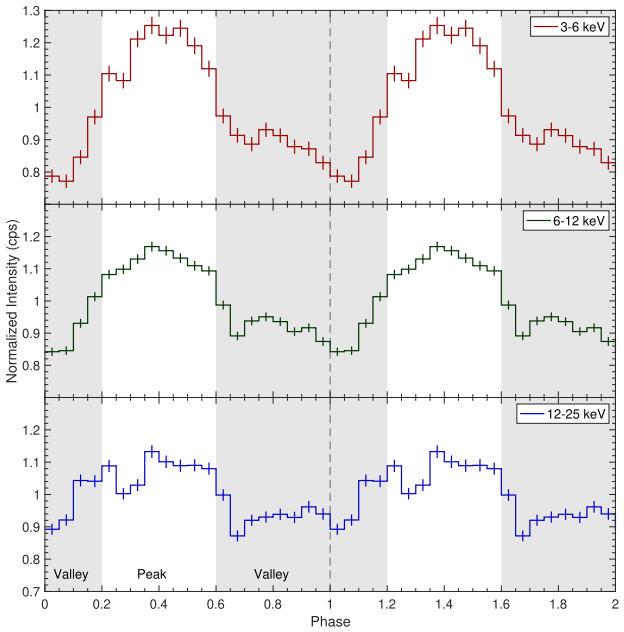

Figure 4. Pulse profiles ($P = 1308.8$ s) in three energy bands from the NuSTAR observation. The pulse is repeated once for ease of viewing. Bins attributed to the peak (white, phases 0.2–0.6) and to the valley (gray, phases 0.0–0.2 and 0.6–1.0) are designated for phase-resolved spectroscopy. All panels have the same vertical scale.

Featuring a single broad peak and a mirrored valley, the shape of the pulse profile from this 2015 NuSTAR observation is similar to the one from 2004 using XMM-Newton and INTEGRAL (Rodriguez et al. 2006). However, there was a significant difference in the pulsed fraction between the observations. The pulsed fraction is defined as $(I_{\rm max} - I_{\rm min})/(I_{\rm max} + I_{\rm min})$, where $I_{\rm max}$ and $I_{\rm min}$ are the normalized count rates in the highest-intensity bin (phase: 0.35–0.40) and lowest-intensity bin (phase: 0.0–0.05), respectively. Figure 5 shows that the pulsed fraction decreased significantly as a function of energy during this NuSTAR observation. The rms of the NuSTAR light curves had a similar negative correlation with energy. This behavior is different from what was previously seen by XMM-Newton and INTEGRAL, where the pulsed fraction was consistent with being constant as a function of energy (Rodriguez et al. 2006).

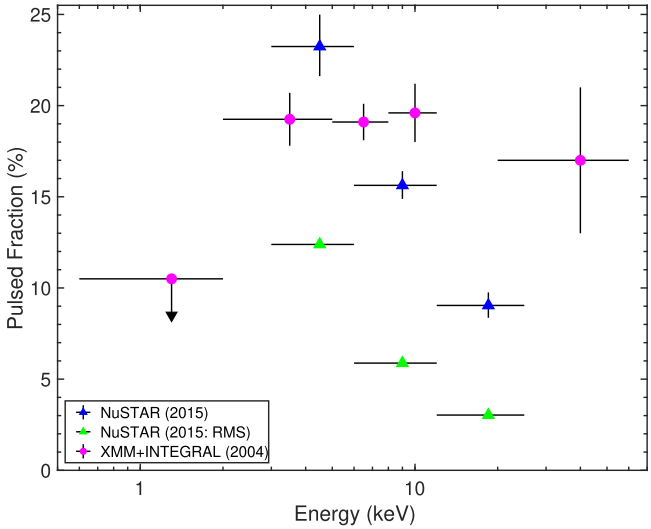

Figure 5. Energy dependence of the pulsed fraction. The pulsed fractions of the IGR J16320−4751 light curves are shown for the 2015 NuSTAR observation (blue; $P = 1308.8$ s) and for the 2004 observation by Rodriguez et al. (2006) combining XMM-Newton and INTEGRAL (magenta; $P = 1303$ s). The rms values of the NuSTAR light curves (green) are also plotted as a reference.

3.1.3. Orbital Period

The 17 yr BAT light curve of IGR J16320−4751 illustrates the stability of the source flux on timescales of years, as shown in the main panel of Figure 6. The figure reveals a prominent flare around MJD 58,500, where, over the course of 2–3 months, the source count rate increased up to a factor of nearly 20 to 7.4×10^{-2} cts cm^{-2} s^{-1} from a mean value (without the flare) of 3.8×10^{-3} cts cm^{-2} s^{-1}. We used `efsearch` with 20 bins per period and a resolution of 50 s to generate a periodogram (upper inset panel of Figure 6), and we fit its peak with a Gaussian to obtain an orbital period of 8.9912 ± 0.0078 days with T_{ϕ_0}= MJD 59,760.449555 corresponding to the phase bin with the lowest flux in the folded light curve (lower inset panel of Figure 6). This means the NuSTAR observation coincided with orbital phases 0.97–1.0 and 0.0–0.11. The orbital period matches the value obtained by García et al. (2018) at a higher significance thanks to five additional years of data.

3.2. Spectral Analysis

3.2.1. Phase-averaged Spectroscopy

The spectral data from FPMA and FPMB were collected so that each bin had a signal-to-noise ratio of at least 10. These spectra were initially fit with a power law attenuated by a photoelectric absorption component at low energies (`Tbabs`) and an exponential cutoff at high energies (`CutoffPL`). An instrumental constant (`Const`) was fixed at 1 for FPMA and

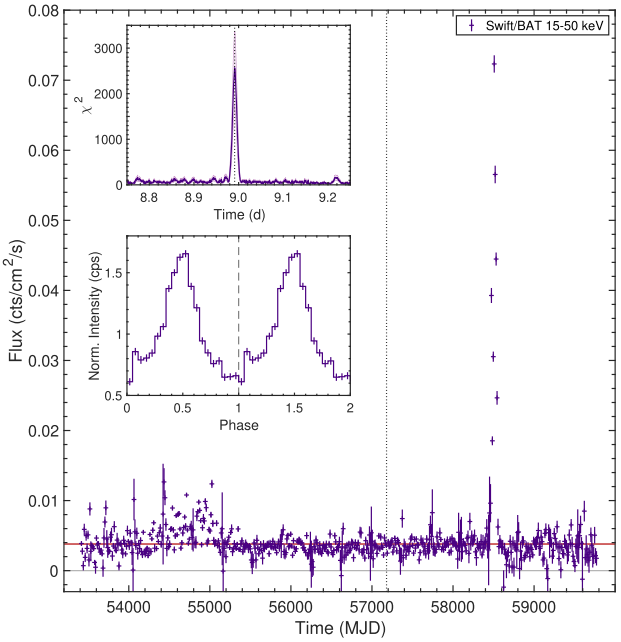

Figure 6. Light curve and orbital period search from Swift/BAT Transient Monitor (Krimm et al. 2013) data of IGR J16320−4751 at 15–50 keV. The main panel presents the count rates at which each bin collects 1 Ms of exposure time. The average count rate (3.8×10^{-3} cts cm^{-2} s^{-1}), which excludes the prominent flare (whose apex occurs on MJD 58,505), is denoted as a horizontal red line. The dotted line indicates the time of the NuSTAR observation. The upper inset panel shows results from an orbital period search centered at 8.9912 days (dotted vertical line), with 20 bins per period and a resolution of 50 s, while the lower inset panel gives two cycles of the orbital period.

allowed to vary for FPMB. This constant was 0.95 ± 0.01 in all cases except for the flare epoch, where it was 0.96 ± 0.02. This spectral model was called "Model 1" (M1), and it left positive residuals around 6.4 keV attributable to an iron Kα line often seen in HMXBs with supergiant donors.

A Gaussian to account for the iron line was then included as "Model 2" (M2). The improvement in fit quality was significant with χ^2_ν/d.o.f. dropping from 1.40/930 in M1 to 1.16/927 in M2 for the full observation. A similar improvement was seen in the nonflare epoch with χ^2_ν/d.o.f. decreasing from 1.35/873 in M1 to 1.13/870 in M2.

The addition of a cyclotron line (`cyclabs`; Makishima et al. 1990; Mihara et al. 1990) in "Model 3" (M3) to account for negative residuals at 10–20 keV led to a slight decrease in χ^2_ν/d.o.f. to 1.12/924 for the full observation. For the nonflare spectrum, the inclusion of the cyclotron component led to a significant improvement in the fit quality with χ^2_ν/d.o.f. reduced to 1.07/867.

Figure 7 presents the NuSTAR spectra from the full observation (left column) and from the nonflare epoch (right column) with the best-fitting model (M3), as well as the residuals from models that gradually included more components. The model parameters are listed in Table 2.

During the nonflare epoch, the best-fitting spectral parameters from M3 were a column density $N_{\rm H} = (10.5 \pm 1.6) \times 10^{22}$ cm^{-2}, a photon index $\Gamma = -0.08^{+0.10}_{-0.11}$, and a cutoff energy $E_{\rm cut} = 11.9^{+2.4}_{-2.1}$ keV. The energy and width of the iron line were $6.28^{+0.06}_{-0.07}$ keV and 0.50 ± 0.08 keV, respectively. The cyclotron line had a centroid energy of $E_{\rm cyc} = 14.3^{+0.9}_{-1.2}$ keV with a width of $\sigma = 4.2^{+1.4}_{-1.2}$ keV and a low optical depth $\tau = 0.10 \pm 0.02$. Confidence contours for the continuum and cyclotron resonance scattering feature (CRSF) parameters are shown in Figure 8.

Models with a high-energy cutoff (`highecut`; White et al. 1983), a negative and positive power-law exponential (`NPEX`; Makishima et al. 1999), a reflection component (`reflect`; Magdziarz & Zdziarski 1995), thermal Comptonization (`compTT` and `nthComp`; Titarchuk 1994; Zdziarski et al. 1996; Życki et al. 1999), and a Fermi–Dirac cutoff (`FDcut`; Tanaka 1986) were also attempted. None of them provided a significant improvement over M3.

There were too few counts in Swift/XRT (∼100) to be useful for our spectral analysis. Fitting the Swift 0.5–10 keV spectrum by itself with an absorbed power law led to unconstrained parameters, whether grouping to a minimum of 20 counts per bin, or leaving the counts unbinned and using Cash (1979) statistics. Jointly fitting the Swift and NuSTAR spectra returned an instrumental constant ∼4 for NuSTAR, even during the nonflare epoch. Depending on the epoch, fits to the combined Swift and NuSTAR spectra at 0.5–79 keV gave a column density of (16–21) $\times$ 10^{22} cm^{-2}. Since this was consistent with the values we obtained when relying on NuSTAR alone, as well as with the values cited by Rodriguez et al. (2006) and by García et al. (2018), the Swift spectral data were no longer included in the analysis.

The significance of the cyclotron line was estimated using the F-statistic (e.g., Orlandini et al. 2012; Sartore et al. 2015; Brumback et al. 2018). The `XSpec` script `fakeit` was used to simulate 2×10^6 spectra based on the model representing the null hypothesis, i.e., an absorbed, cutoff power law with an iron line but without a `cyclabs` component (the "null model" or M2). Each simulated spectrum was binned in the same way as the observed data set and fit with the null model, and its χ^2 was recorded. Then, each simulated spectrum was fit with the "best-fitting model" (M3), which was the null model plus a `cyclabs` component whose parameters were allowed to vary within the 90% confidence region of the best-fitting values, and its χ^2 was noted. These simulations yielded a distribution of reduced (i.e., normalized by the d.o.f.) ratios $F_{\rm stat} = \chi^2_0/\chi^2_1$, where the subscripts 0 and 1 denote the null model (M2) and the best-fitting model (M3), respectively. Every ratio from the simulations was less than the observed $F_{\rm stat} = 1.051$ with the largest simulated value being $F_{\rm stat} = 1.033$. From this distribution, we infer that the cyclotron line was significant at a level of at least 5σ after accounting for the number of trials.

3.2.2. Phase-resolved Spectroscopy

We performed phase-resolved spectroscopy focusing only on data from the nonflare epoch. The pulse profile was split according to phases belonging to the "valley" (phases: 0–0.2, 0.6–1.0) and "peak" (phases: 0.2–0.6) as shown in Figure 4. This allocated a total of $105{,}410 \pm 325$ net counts to the valley in 28.85 ks of effective exposure time, and $75{,}516 \pm 557$ net counts to the peak in 18.78 ks of effective exposure time, when summing the counts from both modules.

Figure 9 presents the phase-resolved spectra fit with the three models introduced earlier, and Table 3 lists the model parameters. M3 continued to provide the best fit. Count rates and model-derived fluxes were between 10% and 20% higher during the peak than they were during the valley, which is consistent with the pulsed fraction. Figure 10 shows the confidence regions for the continuum and CRSF parameters during the peak and valley phases.

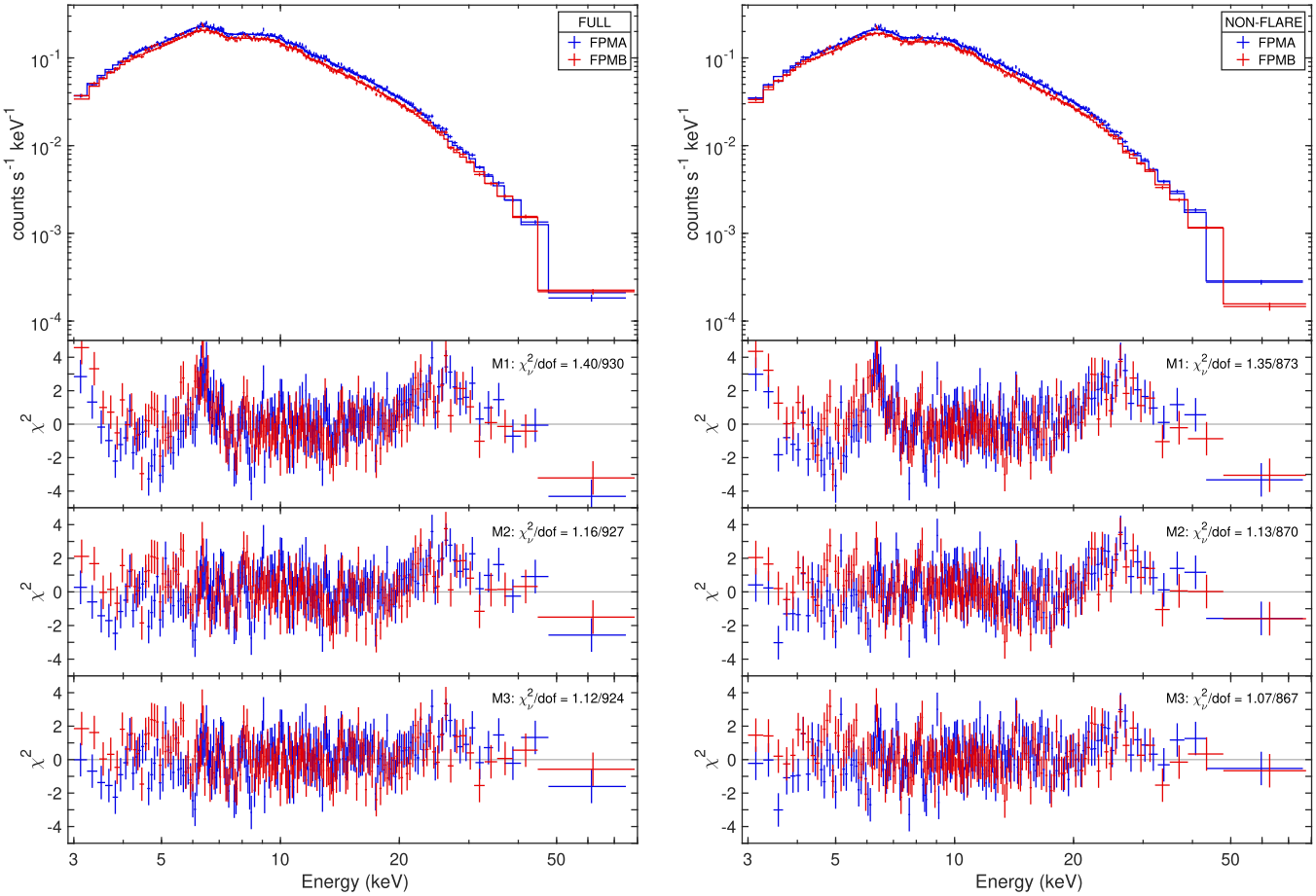

Figure 7. Phase-averaged NuSTAR spectra for IGR J16320−4751. The column of panels on the left presents the background-subtracted source spectrum from the full observation, while the column of panels on the right features the spectrum restricted to the nonflare epoch as defined in Figure 2. Within each column, the top panel contains the spectral data and the best-fitting model (M3), while the lower rows of panels show residuals from fitting the three `CutoffPL`-based models listed in Table 2. Each bin collects a minimum significance of 20σ to better highlight deviations from the model (compared with 10σ during fits).

During the valley phase, there were negative residuals in the spectral fits for the 30–35 keV energy range. This energy is a little higher than would be expected for the harmonic to a candidate cyclotron line at 15 keV. Introducing a second cyclotron component did not reduce the χ^2, and the component's parameters could not be constrained without holding the others constant. This dip was not observed in the spectral residuals during the peak phase.

4. Discussion

The unusual properties of obscured, slowly rotating pulsars such as IGR J16320−4751 trace their origin to the interaction between the NS's magnetosphere and the inhomogeneous accretion stream from the stellar wind (e.g., Grebenev & Sunyaev 2007; Patel et al. 2007; Bozzo et al. 2008; Manousakis et al. 2012; Oskinova et al. 2012; Hainich et al. 2020). The magnetic field strength (B) of the NS can be directly measured by observing CRSFs, which are generally observed as absorption lines between 10 and 100 keV. They arise through resonant scattering of photons emitted by electrons that move perpendicularly to the B-field and whose energies (E) are discretized into integer multiples of the fundamental Landau level: $E_{\rm cyc} \sim 12(B/10^{12}\ {\rm G})$ keV (Truemper et al. 1978; Coburn et al. 2002).

Thanks to NuSTAR, we were able to perform a spectroscopic study of IGR J16320−4751 with unprecedented energy resolution and sensitivity above 10 keV. A spectral model consisting of an absorbed power law left residuals near the known iron Kα line energy of 6.4 keV. However, there were also residuals around 14 keV due to a possible CRSF. The addition of a cyclotron line to the model improved the fit quality enough that the distribution of F-statistics implied a detection significance of 5σ. The energy of the candidate cyclotron line was close to, but not statistically compatible with, the cutoff energy. Plus, in every instance of our simulated spectra, a model that included a cutoff and a cyclotron led to a better fit than a model with a cutoff alone. One alternative is that the candidate cyclotron line is an example of the "10 keV bump" noted in other accreting X-ray pulsars (Coburn et al. 2002; Ferrigno et al. 2009). However, a model in which the cyclotron line was replaced with a Gaussian emission line or a Compton hump led to a poorer-quality fit. As an additional test, we followed the procedure in Bottacini (2022) where the cyclotron energy was stepped in increments of 0.4 keV (NuSTAR's energy resolution) through the full 3–79 keV band, until the best fit was obtained based on χ^2. Once again, the cyclotron was detected significantly around 14 keV (according to the reduced F-statistic distribution) and away from the cutoff energy and the possible bump. A cyclotron line energy of 14 keV corresponds to a B-field magnitude of 1.2×10^{12} G, neglecting the gravitational redshift of the emission region. This is the first time that the magnetic field

Table 2
Parameters from Different Empirical Models Fit to NuSTAR Spectra of IGR J16320−4751

	Flare	Nonflare	Full	Nonflare	Full	Nonflare	Full
		M1		M2		M3	
				photoelectric absorption (Tbabs)			
$N_{\rm H}$[a]	$11.7^{+2.6}_{-2.5}$	19.4 ± 0.9	18.0 ± 0.9	13.4 ± 1.2	12.2 ± 1.1	10.5 ± 1.6	10.4 ± 1.4
				cutoff power law (CutoffPL)			
Γ	-0.04 ± 0.12	0.48 ± 0.04	0.39 ± 0.04	0.18 ± 0.06	0.09 ± 0.06	$-0.08^{+0.10}_{-0.11}$	$-0.09^{+0.09}_{-0.10}$
$E_{\rm cut}$[b]	$11.6^{+1.0}_{-0.8}$	$15.2^{+0.6}_{-0.5}$	$14.3^{+0.5}_{-0.4}$	12.7 ± 0.5	12.1 ± 0.4	11.0 ± 0.6	$10.9^{+0.6}_{-0.5}$
$f_{\rm cut}$[c]	$37.9^{+9.5}_{-7.6}$	$34.4^{+2.9}_{-2.7}$	$31.7^{+2.5}_{-2.3}$	$18.5^{+2.4}_{-2.2}$	$17.2^{+2.0}_{-1.9}$	$11.9^{+2.4}_{-2.1}$	$12.6^{+2.4}_{-2.1}$
				Fe Kα line (Gauss)			
$E_{\rm Fe}$[b]	...	...	...	6.34 ± 0.06	6.34 ± 0.06	$6.28^{+0.06}_{-0.07}$	$6.30^{+0.08}_{-0.07}$
$\sigma_{\rm Fe}$[b]	...	...	...	0.44 ± 0.08	0.46 ± 0.08	0.50 ± 0.08	0.48 ± 0.09
$f_{\rm Fe}$[c]	...	...	...	$1.96^{+0.34}_{-0.32}$	$2.12^{+0.36}_{-0.33}$	$2.31^{+0.43}_{-0.40}$	$2.27^{+0.43}_{-0.41}$
				CRSF (cyclabs)			
$E_{\rm cyc}$[b]	...	...	...	...	...	$14.3^{+0.9}_{-1.2}$	$13.4^{+1.0}_{-2.0}$
$\sigma_{\rm cyc}$[b]	...	...	...	...	...	$4.2^{+1.4}_{-1.2}$	$4.3^{+2.1}_{-1.4}$
$\tau_{\rm cyc}$[d]	...	...	...	...	...	0.10 ± 0.02	$0.08^{+0.03}_{-0.02}$
χ^2_ν (d.o.f.)	1.17 (224)	1.35 (873)	1.40 (930)	1.13 (870)	1.16 (927)	1.07 (867)	1.12 (924)
F[e]	$26.46^{+0.33}_{-1.15}$	$8.85^{+0.05}_{-0.08}$	$9.65^{+0.06}_{-0.07}$	$8.91^{+0.05}_{-0.11}$	$9.72^{+0.05}_{-0.10}$	$8.97^{+0.04}_{-0.30}$	$9.78^{+0.04}_{-0.27}$

Notes.
[a] Equivalent hydrogen column density ($\times 10^{22}$ cm^{-2}).
[b] In keV.
[c] Normalization at 1 keV ($\times 10^{-4}$ ph s^{-1} cm^{-2} keV^{-1}).
[d] Optical depth.
[e] Model-derived flux in the 2–10 keV band ($\times 10^{-11}$ erg s^{-1} cm^{-2}).

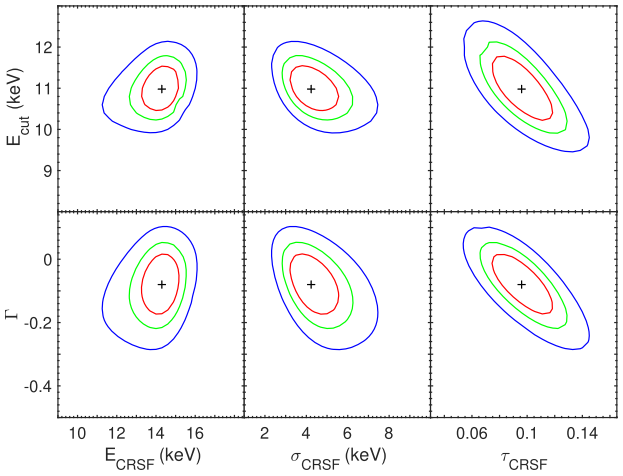

Figure 8. Confidence regions for the cyclotron parameters from the best-fitting spectral model (M3) during the nonflare epoch. Red, green, and blue lines represent 68%, 90%, and 99% confidence contours, respectively, around the optimal value shown as a cross.

of this source has been measured. It is not particularly strong compared with that of its peers (Staubert et al. 2019).

Cyclotron lines show variability with luminosity and pulse phase, and are often most significantly detected during certain phases (e.g., Suchy et al. 2012). The candidate cyclotron line in IGR J16320−4751 was easier to detect during the nonflare epoch, and during the valley when analyzing by phase. We saw no evidence of an increase in the line energy with pulse phase, as was seen in Her X-1 (e.g., Soong et al. 1990; Vasco et al. 2013), nor were there significant negative/positive correlations with luminosity (Staubert et al. 2019, and references therein).

The cyclotron scattering cross section and by extension the optical depth are strongly affected by the viewing angle relative to the axis defined by the magnetic field (e.g., Schwarm et al. 2017a, 2017b). The optical depth of $\tau_{\rm cyc} = 0.1$ in IGR J16320−4751 is lower than those of the 10 other sources reported in Coburn et al. (2002), which range from 0.16 to 2.1. Also, the ratio of width to energy ($\sigma_{\rm cyc}/E_{\rm cyc} = 0.3$) that we measured is more than twice as high as expected based on the trend found in Coburn et al. (2002), where deeper CRSFs tended to be broader (Figure 11). On the other hand, our values for IGR J16320−4751 occupy a region of the parameter space that was inaccessible to the systematic study of RXTE data by Coburn et al. (2002), but that can now be explored by NuSTAR, which we did by adding 12 more HMXBs listed in Staubert et al. (2019), and references therein. Whereas IGR J16320−4751 was once an outlier compared with the HMXBs of Coburn et al. (2002), it now has company in that it overlaps statistically with IGR J18027−2016 and KS 1947 + 300. Both of them had many years pass between their discovery (Borozdin et al. 1990; Augello et al. 2003) and the detection of weak cyclotron lines by NuSTAR (Fürst et al. 2014a; Lutovinov et al. 2017).

A coherent modulation with a period of 1308.8 ± 0.4 s was measured by NuSTAR. This is known to be the spin period of the NS in IGR J16320−4751. Rodriguez et al. (2006) found an average value of 1303 s between two separate XMM-Newton observations from 2004, while García et al. (2018) reported a period of ∼1300 s from XMM-Newton observations between 2003 and 2008. Assuming there was no torque reversal (Bildsten et al. 1997), a 5.8 s difference between measurements from 2004 and 2015 (3943 days) indicates a spin-down trend with a period derivative $\dot{P} \sim 2 \times 10^{-8}$ s s^{-1}. Attributing the slowing down of the NS to magnetic braking or propellor

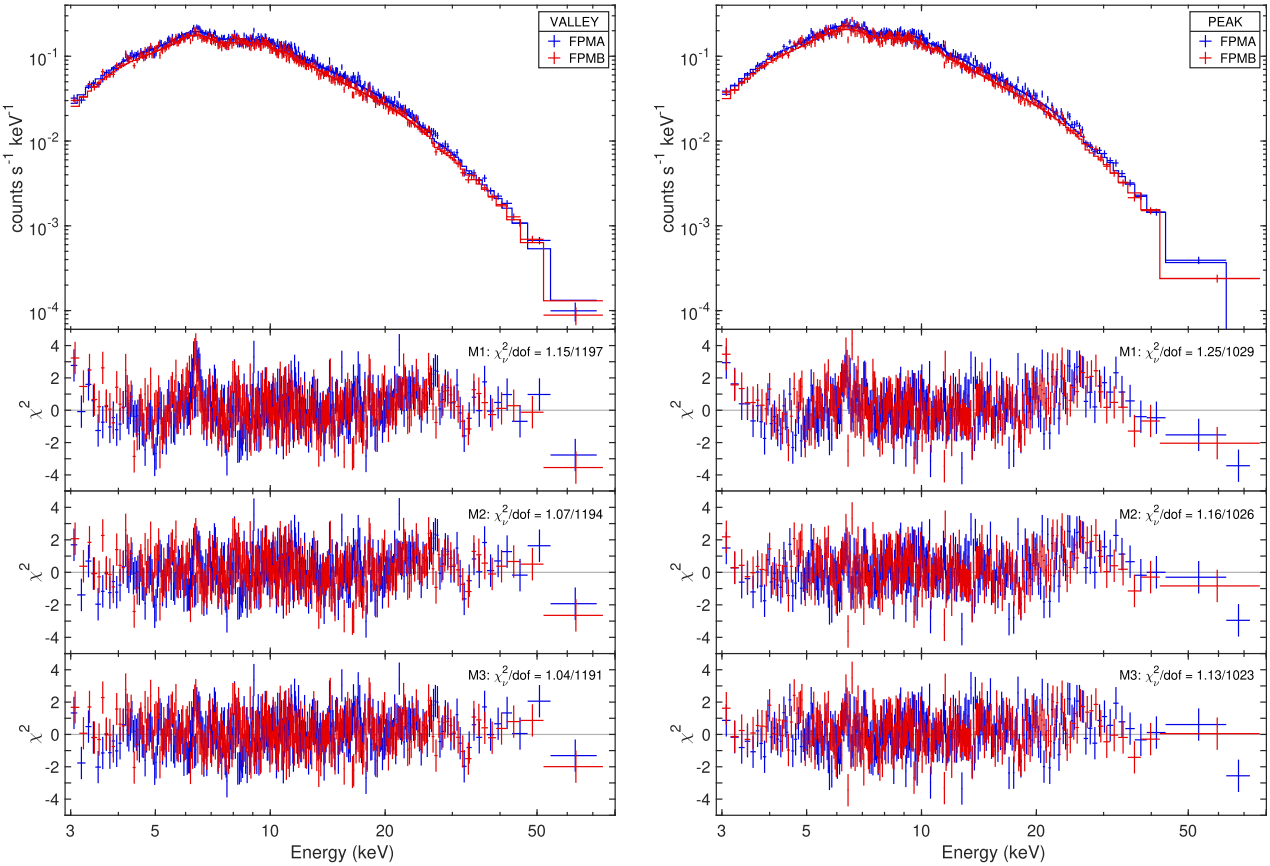

Figure 9. Phase-resolved NuSTAR spectra for IGR J16320−4751 from FPMA (blue) and FPMB (red) during the nonflare epoch. The column of panels on the left shows the source spectrum during the valley phases defined in Figure 4, while the column of panels on the right shows data from the peak phase. In each column, the top row shows the spectrum and best-fitting model (M3), while the second, third, and fourth rows present the residuals from fitting the models listed in Table 3. For visual clarity, the spectra were rebinned to a minimum significance of 10σ (compared with 5σ during fits).

effects (Illarionov & Sunyaev 1975) would require a higher magnetic field strength and pulsation frequency than what we measured for IGR J16320−4751. The accretion of material with negative angular momentum appears to be the most likely explanation, and this could proceed either through an inhomogeneous stellar wind (Shakura et al. 2012), or via a short-lived accretion disk. In addition to provoking outbursts in the SFXT IGR J17544−2619 (Romano et al. 2015), transient accretion disks may explain long-term changes in the spin period of other HMXBs with supergiant stars such as OAO 1657−415 (Jenke et al. 2012) and IGR J16393−4643 (Bodaghee et al. 2016). The spin period derivatives of IGR J16320−4751 and IGR J16393−4643 are equal in magnitude, but unequal in direction: the former is slowing down while the latter is speeding up.

The pulsation was detected in every energy band that we analyzed except for 25–79 keV, where few counts remained since the spectral continuum decayed exponentially at $\gtrsim$10 keV. The pulsed fraction at 3–6 keV was twice as large as that at 12–25 keV, which is surprising given that the pulsed fraction stayed constant with energy in 2004. It is also surprising given that in accreting X-ray pulsars, the pulsed fraction tends to increase with energy (Nagase 1989; Bildsten et al. 1997; Mushtukov & Tsygankov 2022). This suggests a physical change in the system in the intervening 11 yr, which could include, for example, a reconfiguration of the magnetic field, a change in the energy dependence over the beam, or a change in beam pattern or size. The low significance and low pulsed fraction of the modulation at energies above 10 keV could explain the weakness of the candidate cyclotron line.

IGR J16320−4751 is a persistent X-ray source with a count rate that stayed relatively constant over almost 2 decades of Swift/BAT monitoring at 15–50 keV (Krimm et al. 2013). Still, the source experienced small flares with the largest flare reaching a count rate 20 times the average. An orbital modulation with a refined period of 8.9912 ± 0.0078 days was found, in agreement with previous measurements (Corbet et al. 2005; Levine et al. 2011; García et al. 2018). The NuSTAR observation covered orbital phases 0.97–0.11, where phase 0 (= 1) represents the minimum point of the orbital profile. By extension, the NuSTAR observation occurred close to superior conjunction, i.e., when the X-ray-emitting NS was furthest in its orbit with respect to the observer. With an eccentricity of 0.2 and an inclination angle of 62° (García et al. 2018), the source is not eclipsing so attenuation of X-rays at this phase is likely due to absorption by the companion star's wind. The XMM-Newton observation of Rodriguez et al. (2006) coincided with phases 0.40–0.46, i.e., just before the maximum point of the orbital profile, or near inferior conjunction.

The unabsorbed 2–10 keV flux reported by Rodriguez et al. (2006) during their nonflare epoch is 9.2×10^{-11} erg cm^{-2} s^{-1}, which is equivalent to the absorption-corrected flux for the nonflare epoch that we found with NuSTAR: 1.1×10^{-10} erg cm^{-2} s^{-1}. This is somewhat surprising given that the 2004 XMM-Newton and 2015 NuSTAR observations occurred, respectively, near the highest and lowest points in the orbital profile. However,

Table 3
Fitting Parameters of the Phase-resolved Nonflare Spectra of IGR J16320−4751 with Three Empirical Models

	Valley	Peak	Valley	Peak	Valley	Peak
	M1		**M2**		**M3**	
			photoelectric absorption (Tbabs)			
N_H [a]	18.2 ± 1.2	20.9 ± 1.4	$13.3^{+1.6}_{-1.5}$	$13.5^{+2.0}_{-1.9}$	10.5 ± 1.9	$8.4^{+3.3}_{-3.5}$
			cutoff power law (CutoffPL)			
Γ	0.37 ± 0.05	0.60 ± 0.06	0.13 ± 0.08	0.22 ± 0.11	-0.10 ± 0.12	$-0.25^{+0.21}_{-0.28}$
E_{cut} [b]	$14.6^{+0.7}_{-0.6}$	14.9 ± 0.8	$12.7^{+0.7}_{-0.6}$	$11.9^{+0.8}_{-0.7}$	11.2 ± 0.7	$9.6^{+0.9}_{-1.0}$
f_{cut} [c]	$25.9^{+2.9}_{-2.6}$	$49.5^{+6.5}_{-5.6}$	$15.8^{+2.8}_{-2.2}$	$22.2^{+5.2}_{-4.4}$	$10.4^{+2.6}_{-2.1}$	$9.8^{+4.7}_{-4.0}$
			Fe Kα line (Gauss)			
E_{Fe} [b]	...	...	6.34 ± 0.07	6.31 ± 0.11	6.30 ± 0.07	$6.14^{+0.32}_{-0.14}$
σ_{Fe} [b]	...	...	$0.34^{+0.10}_{-0.14}$	$0.64^{+0.16}_{-0.15}$	$0.40^{+0.09}_{-0.10}$	$0.74^{+0.18}_{-0.30}$
f_{Fe} [c]	...	...	$1.45^{+0.36}_{-0.38}$	$3.11^{+0.89}_{-0.76}$	$1.77^{+0.39}_{-0.38}$	$4.17^{+1.63}_{-1.87}$
			CRSF (cyclabs)			
E_{CRSF} [b]	...	...	...	...	15.1 ± 1.0	$13.8^{+2.8}_{-3.3}$
σ_{CRSF} [b]	...	...	...	...	$3.9^{+1.7}_{-1.4}$	$5.8^{+3.9}_{-3.2}$
τ_{CRSF} [d]	...	...	...	...	0.10 ± 0.03	$0.15^{+0.11}_{-0.05}$
χ^2_{red} (d.o.f.)	1.15 (1197)	1.25 (1029)	1.07 (1194)	1.16 (1026)	1.04 (1191)	1.13 (1023)
F [e]	$8.25^{+0.06}_{-0.10}$	$9.67^{+0.08}_{-0.16}$	$8.29^{+0.06}_{-0.14}$	$9.75^{+0.07}_{-0.31}$	$8.35^{+0.05}_{-0.36}$	$9.85^{+0.04}_{-0.50}$

Notes.
[a] Equivalent hydrogen column density ($\times 10^{22}$ cm^{-2}).
[b] In keV.
[c] Normalization at 1 keV ($\times 10^{-4}$ ph s^{-1} cm^{-2} keV^{-1}).
[d] Optical depth.
[e] Model-derived flux in the 2–10 keV band ($\times 10^{-11}$ erg s^{-1} cm^{-2}).

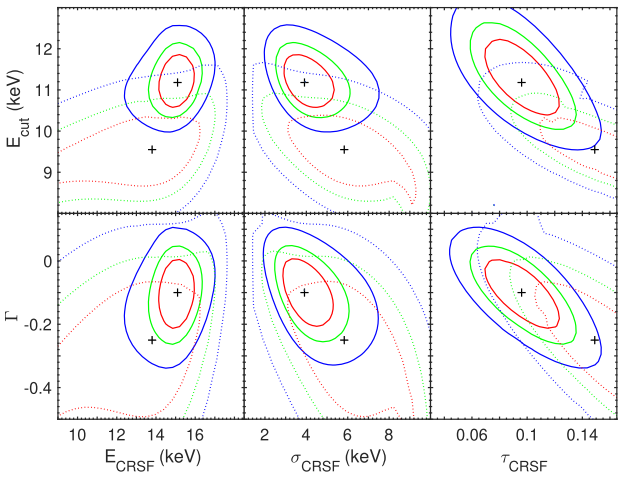

Figure 10. Same as Figure 8, with identical limits for the axes, but for phases corresponding to the peak (dotted lines) and the valley (solid lines).

García et al. (2018) reported on a 2008 XMM-Newton observation taken during phase 0 where the flux was 2.17×10^{-10} erg cm^{-2} s^{-1} (0.15–12 keV), so the flux discrepancy is probably due to the stochastic variability of the source.

Based on infrared spectroscopy of the counterpart to IGR J16320−4751, Rahoui et al. (2008) estimated a source distance of 3.5 kpc. At this distance, the intrinsic (i.e., absorption-corrected) 2–10 keV source luminosity would be 1.7×10^{35} erg s^{-1} outside the flare, and 5.1×10^{35} erg s^{-1} during the flare. No objects listed in the Gaia DR3 (Gaia Collaboration et al. 2016, 2021) catalog of parallax-derived distances (Bailer-Jones et al. 2021) were within 5″ of the 4XMM position of IGR J16320−4751. If we assume a distance of 10 kpc instead, then the luminosities during the nonflare and flare epochs would be 1.4×10^{36} erg s^{-1} and 4.2×10^{36} erg s^{-1}, respectively.

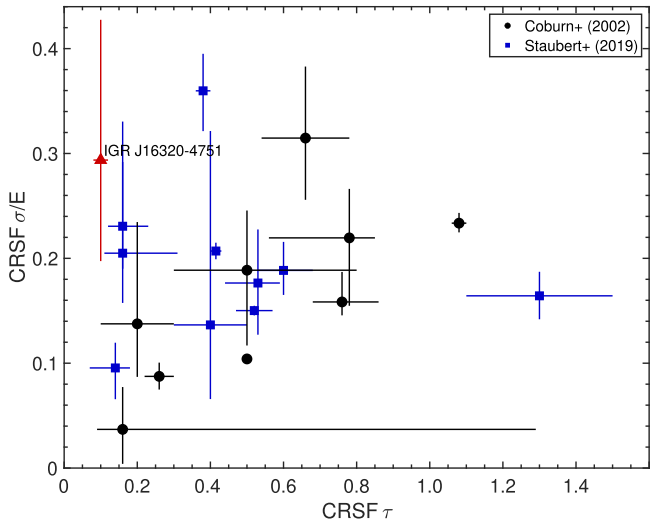

Figure 11. Relative width (σ/E) vs. optical depth (τ) of the CRSF (adapted from Coburn et al. 2002). The location of IGR J16320−4751 in the parameter space is indicated by the red triangle, while other HMXBs appear as black circles (from Coburn et al. 2002) or blue squares (from Staubert et al. 2019, and references therein).

5. Conclusions

NuSTAR gave an exclusive look at the accreting X-ray pulsar IGR J16320−4751 in an energy band above 10 keV that has not been covered with as fine a spectral resolution with other telescopes. The spectrum of IGR J16320−4751 was best fit by introducing a CRSF at ∼14 keV in addition to a cutoff power-law

continuum and an Fe Kα line. If confirmed, the cyclotron line would represent the first direct measurement of a 1.2×10^{12} G magnetic field for the NS in IGR J16320−4751. In this 2015 study, the pulsed fraction showed a significant negative correlation with energy, whereas the pulsed fraction remained constant in 2004. This suggests that the system's magnetically driven accretion geometry changed between the observations.

NuSTAR provided new insights into the evolution of line properties on long and short timescales in HMXBs known to have CRSFs, e.g., Her X-1 and Vela X-1 (Fürst et al. 2013, 2014b). NuSTAR has also uncovered cyclotron lines for HMXBs not previously known to have them (e.g., Fürst et al. 2014a; Tendulkar et al. 2014; Bhalerao et al. 2015; Bodaghee et al. 2016). With ∼35 known CRSF sources, including candidate cyclotron sources, of which IGR J16320−4751 is now a member, the increasing sample size will permit studies of the relationship between the *B*-field and other properties, such as luminosity, companion type, spin period, and orbital period (e.g., Schönherr et al. 2014; Christodoulou et al. 2019; Staubert et al. 2019).

Acknowledgments

J.A.T. and J.-L.C. acknowledge partial support from NASA grant NNX15AV22G under the NuSTAR Guest Observer program. M.C. acknowledges financial support from Centre National d'Etudes Spatiales (CNES). P.R. acknowledges financial contributions from the agreements ASI-INAF I/037/12/0 and ASI-INAF No. 2017-14-H.0. The scientific results reported in this article are based on data from the NuSTAR mission, a project led by the California Institute of Technology, managed by the Jet Propulsion Laboratory, and funded by the National Aeronautics and Space Administration. This research has made use of the NuSTAR Data Analysis Software (NuSTARDAS) jointly developed by the ASI Science Data Center (ASDC, Italy) and the California Institute of Technology; data obtained from the High Energy Astrophysics Science Archive Research Center (HEASARC) provided by NASA's Goddard Space Flight Center; NASA's Astrophysics Data System Bibliographic Services; and the SIMBAD database operated at CDS, Strasbourg, France.

Facilities: NuSTAR, Swift (XRT and BAT).

Software: HEASoft v6.29 (Nasa High Energy Astrophysics Science Archive Research Center (Heasarc) 2014), FTOOLS v6.29 (Blackburn et al. 1999), NuSTARDAS v2.1.1, XSpec v12.12.0 (Arnaud 1996), Matlab R2021b (MATLAB 2021).

ORCID iDs

A. Bodaghee https://orcid.org/0000-0002-7315-3732
J. A. Tomsick https://orcid.org/0000-0001-5506-9855
V. Bhalerao https://orcid.org/0000-0002-6112-7609
M. Clavel https://orcid.org/0000-0003-0724-2742
F. Fürst https://orcid.org/0000-0003-0388-0560
M. J. Middleton https://orcid.org/0000-0002-8183-2970
F. Rahoui https://orcid.org/0000-0001-7655-4120
J. Rodriguez https://orcid.org/0000-0002-4151-4468
P. Romano https://orcid.org/0000-0003-0258-7469
J. Wilms https://orcid.org/0000-0003-2065-5410

References

Abdollahi, S., Acero, F., Ackermann, M., et al. 2020, ApJS, 247, 33
Acero, F., Ackermann, M., Ajello, M., et al. 2015, ApJS, 218, 23
Aharonian, F., Akhperjanian, A. G., Bazer-Bachi, A. R., et al. 2006, ApJ, 636, 777
Arnaud, K. A. 1996, in ASP Conf. Ser. 101, Astronomical Data Analysis Software and Systems V, ed. G. H. Jacoby & J. Barnes (San Francisco, CA: ASP), 17
Augello, G., Iaria, R., Robba, N. R., et al. 2003, ApJL, 596, L63
Bailer-Jones, C. A. L., Rybizki, J., Fouesneau, M., Demleitner, M., & Andrae, R. 2021, AJ, 161, 147
Bhalerao, V., Romano, P., Tomsick, J., et al. 2015, MNRAS, 447, 2274
Bildsten, L., Chakrabarty, D., Chiu, J., et al. 1997, ApJS, 113, 367
Blackburn, J. K., Shaw, R. A., Payne, H. E., Hayes, J. J. E., & Heasarc 1999, FTOOLS: A general package of software to manipulate FITS files, Astrophysics Source Code Library, ascl:9912.002
Bodaghee, A., Tomsick, J. A., Fornasini, F. M., et al. 2016, ApJ, 823, 146
Bodaghee, A., Walter, R., Zurita Heras, J. A., et al. 2006, A&A, 447, 1027
Borozdin, K., Gilfanov, M., Sunyaev, R., et al. 1990, SvAL, 16, 345
Bottacini, E. 2022, MNRAS, 515, 3174
Bozzo, E., Falanga, M., & Stella, L. 2008, ApJ, 683, 1031
Bozzo, E., Romano, P., Ducci, L., Bernardini, F., & Falanga, M. 2015, AdSpR, 55, 1255
Brumback, M. C., Hickox, R. C., Fürst, F. S., et al. 2018, ApJ, 852, 132
Cash, W. 1979, ApJ, 228, 939
Christodoulou, D. M., Laycock, S. G. T., & Kazanas, D. 2019, RAA, 19, 146
Coburn, W., Heindl, W. A., Rothschild, R. E., et al. 2002, ApJ, 580, 394
Coleiro, A., Chaty, S., Zurita Heras, J. A., Rahoui, F., & Tomsick, J. A. 2013, A&A, 560, A108
Corbet, R., Barbier, L., Barthelmy, S., et al. 2005, ATel, 649, 1
Ferrigno, C., Becker, P. A., Segreto, A., Mineo, T., & Santangelo, A. 2009, A&A, 498, 825
Fürst, F., Grefenstette, B. W., Staubert, R., et al. 2013, ApJ, 779, 69
Fürst, F., Pottschmidt, K., Wilms, J., et al. 2014a, ApJL, 784, L40
Fürst, F., Pottschmidt, K., Wilms, J., et al. 2014b, ApJ, 780, 133
Gaia Collaboration, Brown, A. G. A., Vallenari, A., et al. 2021, A&A, 649, A1
Gaia Collaboration, Prusti, T., de Bruijne, J. H. J., et al. 2016, A&A, 595, A1
García, F., Fogantini, F. A., Chaty, S., & Combi, J. A. 2018, A&A, 618, A61
Giménez-García, A., Torrejón, J. M., Eikmann, W., et al. 2015, A&A, 576, A108
Grebenev, S. A., & Sunyaev, R. A. 2007, AstL, 33, 149
Hainich, R., Oskinova, L. M., Torrejón, J. M., et al. 2020, A&A, 634, A49
Horne, J. H., & Baliunas, S. L. 1986, ApJ, 302, 757
Illarionov, A. F., & Sunyaev, R. A. 1975, A&A, 39, 185
in't Zand, J. J. M. 2005, A&A, 441, L1
Jenke, P. A., Finger, M. H., Wilson-Hodge, C. A., & Camero-Arranz, A. 2012, ApJ, 759, 124
Kretschmar, P., Fürst, F., Sidoli, L., et al. 2019, NewAR, 86, 101546
Krimm, H. A., Holland, S. T., Corbet, R. H. D., et al. 2013, ApJS, 209, 14
Krivonos, R. A., Sazonov, S. Y., Kuznetsova, E. A., et al. 2022, MNRAS, 510, 4796
Leahy, D. A. 1987, A&A, 180, 275
Levine, A. M., Bradt, H. V., Chakrabarty, D., Corbet, R. H. D., & Harris, R. J. 2011, ApJS, 196, 6
Lomb, N. R. 1976, Ap&SS, 39, 447
Lutovinov, A., Rodriguez, J., Revnivtsev, M., & Shtykovskiy, P. 2005, A&A, 433, L41
Lutovinov, A. A., Tsygankov, S. S., Postnov, K. A., et al. 2017, MNRAS, 466, 593
Magdziarz, P., & Zdziarski, A. A. 1995, MNRAS, 273, 837
Makishima, K., Mihara, T., Ishida, M., et al. 1990, ApJL, 365, L59
Makishima, K., Mihara, T., Nagase, F., & Tanaka, Y. 1999, ApJ, 525, 978
Manousakis, A., Walter, R., & Blondin, J. M. 2012, A&A, 547, A20
2021, MATLAB, V. 9.11.0 (R2021b) (Natick, MA: The MathWorks Inc.)
Matt, G., & Guainazzi, M. 2003, MNRAS, 341, L13
Mihara, T., Makishima, K., Ohashi, T., Sakao, T., & Tashiro, M. 1990, Natur, 346, 250
Mushtukov, A., & Tsygankov, S. 2022, arXiv:2204.14185
Nagase, F. 1989, PASJ, 41, 1
Nasa High Energy Astrophysics Science Archive Research Center (Heasarc) 2014, HEAsoft: Unified Release of FTOOLS and XANADU, Astrophysics Source Code Library, ascl:1408.004
Negueruela, I., Smith, D. M., Reig, P., Chaty, S., & Torrejón, J. M. 2006, in ESA Special Publication, Vol. 604, The X-ray Universe 2005, ed. A. Wilson (Madrid: ESA), 165
Orlandini, M., Frontera, F., Masetti, N., Sguera, V., & Sidoli, L. 2012, ApJ, 748, 86
Oskinova, L. M., Feldmeier, A., & Kretschmar, P. 2012, MNRAS, 421, 2820
Patel, S. K., Kouveliotou, C., Tennant, A., et al. 2004, ApJL, 602, L45

Patel, S. K., Zurita, J., Del Santo, M., et al. 2007, ApJ, 657, 994
Pradhan, P., Bozzo, E., & Paul, B. 2018, A&A, 610, A50
Press, W. H., & Rybicki, G. B. 1989, ApJ, 338, 277
Rahoui, F., Chaty, S., Lagage, P. O., & Pantin, E. 2008, A&A, 484, 801
Rodriguez, J., Bodaghee, A., Kaaret, P., et al. 2006, MNRAS, 366, 274
Rodriguez, J., Tomsick, J. A., Foschini, L., et al. 2003, A&A, 407, L41
Romano, P., Bozzo, E., Mangano, V., et al. 2015, A&A, 576, L4
Romano, P., Krimm, H. A., Palmer, D. M., et al. 2014, A&A, 562, A2
Sartore, N., Jourdain, E., & Roques, J. P. 2015, ApJ, 806, 193
Scargle, J. D. 1982, ApJ, 263, 835
Schönherr, G., Schwarm, F. W., Falkner, S., et al. 2014, A&A, 564, L8
Schwarm, F. W., Ballhausen, R., Falkner, S., et al. 2017a, A&A, 601, A99
Schwarm, F. W., Schönherr, G., Falkner, S., et al. 2017b, A&A, 597, A3
Shakura, N., Postnov, K., Kochetkova, A., & Hjalmarsdotter, L. 2012, MNRAS, 420, 216
Sidoli, L., & Paizis, A. 2018, MNRAS, 481, 2779
Sidoli, L., Paizis, A., & Postnov, K. 2016, MNRAS, 457, 3693
Soong, Y., Gruber, D. E., Peterson, L. E., & Rothschild, R. E. 1990, ApJ, 348, 641
Staubert, R., Trümper, J., Kendziorra, E., et al. 2019, A&A, 622, A61
Suchy, S., Fürst, F., Pottschmidt, K., et al. 2012, ApJ, 745, 124
Sugizaki, M., Mitsuda, K., Kaneda, H., et al. 2001, ApJS, 134, 77
Tanaka, Y. 1986, in IAU Coll. 89: Radiation Hydrodynamics in Stars and Compact Objects, Vol. 255, ed. D. Mihalas & K.-H. A. Winkler (Cambridge: Cambridge Univ. Press), 198
Tendulkar, S. P., Fürst, F., Pottschmidt, K., et al. 2014, ApJ, 795, 154
Titarchuk, L. 1994, ApJ, 434, 570
Tomsick, J. A., Lingenfelter, R., Walter, R., et al. 2003, IAU Circ., 8076, 1
Truemper, J., Pietsch, W., Reppin, C., et al. 1978, ApJL, 219, L105
Vasco, D., Staubert, R., Klochkov, D., et al. 2013, A&A, 550, A111
Verner, D. A., Ferland, G. J., Korista, K. T., & Yakovlev, D. G. 1996, ApJ, 465, 487
Walter, R., Lutovinov, A. A., Bozzo, E., & Tsygankov, S. S. 2015, A&ARv, 23, 2
Walter, R., Rodriguez, J., Foschini, L., et al. 2003, A&A, 411, L427
Webb, N. A., Coriat, M., Traulsen, I., et al. 2020, A&A, 641, A136
White, N. E., Swank, J. H., & Holt, S. S. 1983, ApJ, 270, 711
Wilms, J., Allen, A., & McCray, R. 2000, ApJ, 542, 914
Zdziarski, A. A., Johnson, W. N., & Magdziarz, P. 1996, MNRAS, 283, 193
Zurita Heras, J. A., De Cesare, G., Walter, R., et al. 2006, A&A, 448, 261
Życki, P. T., Done, C., & Smith, D. A. 1999, MNRAS, 309, 561